SAND2018-13088J

Using a Dynamic Substructuring Approach to Model the Effects of Acoustic Damping in Coupled Acoustic-Structure Systems

R. Benjamin Davis *
Assistant Professor
College of Engineering
University of Georgia
Athens, Georgia 30602
Email: ben.davis@uga.edu

Ryan Schultz
Technical Staff
Sandia National Laboratories
Albuquerque, New Mexico 87123
Email: rschult@sandia.gov

Acoustic-structure coupling can substantially alter the frequency response of air-filled structures. Coupling effects typically manifest as two resonance peaks at frequencies above and below the resonant frequency of the uncoupled structural system. Here, a dynamic substrucuring approach is applied to a simple acoustic-structure system to expose how the system response depends on the damping in the acoustic subsystem. Parametric studies show that as acoustic damping is increased, the frequencies and amplitudes of the coupled resonances in the structural response undergo a sequence of changes. For low levels of acoustic damping, the two coupled resonances have amplitudes approximating the corresponding in vacuo resonance. As acoustic damping is increased, resonant amplitudes decrease dramatically while the frequency separation between the resonances tends to increase slightly. When acoustic damping is increased even further, the separation of the resonant frequencies decreases below their initial separation. Finally, at some critical value of acoustic damping, one of the resonances abruptly disappears, leaving just a single resonance. Counterintuitively, increasing acoustic damping beyond this point tends to increase the amplitude of the remaining resonance peak. These results have implications for analysts and experimentalists attempting to understand, mitigate, or otherwise compensate for the confounding effects of acoustic-structure coupling in fluid-filled test structures.

*Address all correspondence to this author.

1 Introduction

Modal testing [1] is a cornerstone of the modern practice of structural dynamics. Often, modal tests are performed on hollow, air-filled test articles. In many cases, the presence of the air-filled cavity is negligible and the resulting structural frequency response functions (FRFs) agree with those produced by corresponding *in vacuo* finite element models. However, if a natural mode of the *in vacuo* structure happens to be spatially similar and in close frequency proximity to one or more uncoupled acoustic modes of the cavity, coupling effects cause the structural FRF to deviate from its *in vacuo* counterpart [2]. In these situations, the frequency response of the coupled system resembles that of a tuned-mass-damper (TMD) [3] where the single structural resonance is split into two resonances appearing at forcing frequencies above and below the *in vacuo* resonant frequency. The natural modes corresponding to the two resonances are coupled, with non-negligible content in both the fluid and structure degrees of freedom [4].

Acoustic-structure resonances can confound model correlation efforts which seek to match experimental results to an *in vacuo* finite element analysis. When faced with this issue, it may be tempting to try to suppress the influence of the fluid by adding damping material to the cavity; however, because of the energy exchange between the coupled modes, this strategy will not recover the *in vacuo* structural response. In fact, the resonant behavior of the system as acoustic damping is increased is not intuitive. In a recent modal test of an air-filled aluminum cylinder, Schultz and Pacini [5] identified a pair of acoustic-structure resonances in the structural FRF. They then found that progressively adding foam to the

Sandia National Laboratories is a multimission laboratory managed and operated by National Technology & Engineering Solutions of Sandia, LLC, a wholly owned subsidiary of Honeywell International Inc., for the U.S. Department of Energy's National Nuclear Security Administration under contract DE-NA0003525.

cylinder's cavity eventually prompted the disappearance of one of the coupled resonances, and observed that the frequency and amplitude of the persisting resonance did not seem to match those belonging to the corresponding *in vacuo* resonance.

To provide insight into the effects of acoustic damping in coupled acoustic-structure systems, this paper considers a simple model—a single degree of freedom (SDOF) piston coupled to a one-dimensional acoustic waveguide. This model is appealing because it allows coupling effects to be described in terms of two parameters—the ratio of the structural mass to the fluid mass, σ, and the ratio of the uncoupled structural and acoustic natural frequencies, η. In systems involving continuous structures, a third parameter describing the spatial similarity between the uncoupled acoustic and structural mode shapes also affects coupling strength [6]. The piston/waveguide model effectively removes the influence of this third parameter from the problem; enabling fundamental acoustic-structure interaction behavior to be observed with more simplicity and generality. An additional benefit of the piston/waveguide model is that its undamped response has been studied previously [7, 8]. This allows the implementation of the present modeling approach to be checked against published results.

The physical mechanisms by which energy is dissipated in acoustic media are complicated. Typical acoustic damping models invoke complex-valued, frequency dependent, impedance boundary conditions. To retain model simplicity and generality, acoustic energy dissipation is modeled here using a viscous damping ratio. While this is a simple and familiar strategy, the consideration of acoustic damping of any sort distinguishes the present study from existing acoustic-structure interaction literature. Most acoustic-structure interaction studies are concerned with the prediction of coupled natural frequencies and modes (see, e.g., Refs. [9–11]). Calculation of the forced response of acoustic-structure systems is much less common. In these rare cases, the system is generally assumed to be either undamped [7] or subject to a modal viscous damping ratio applied at the system level [12]. While the present study is distinct in the realm of acoustic-structure interaction research, analogies can be made to previous work considering the influence of attachment mass damping on the forced response of TMDs [13,14].

The present modeling approach proceeds by first using a Ritz series approximation to calculate the natural frequencies and modes of the acoustic subsystem. Next, the modal representations of the acoustic and the structural subsystems are assembled in a disjoint (i.e., unconstrained) system of equations. This enables the straightforward application of acoustic subsystem damping. A boolean constraint matrix is used to specify displacement compatibility at the fluid-structure interface. After transforming the constraint matrix into modal coordinates, its null space is calculated. The result is a matrix that transforms the disjoint system of equations into a generalized coordinate system where the interface constraints are satisfied. An eigen-analysis in this generalized coordinate system yields the system natural frequencies and modes that are used as inputs in a forced response analysis. This approach, which will be referred to as modal coordinate assembly component mode synthesis (MCA-CMS), incorporates elements from the modern practice of dynamic substructuring [15, 16] and Ginsberg's Ritz series analysis of acoustic-structure systems [7, 8, 17]. The MCA-CMS approach has some appealing features. First, and most importantly to this study, it permits the straightforward assignment of acoustic subsystem damping. It also enables direct and accurate recovery of the acoustic pressure at the fluid-structure interface [7]. Looking ahead to future implementations where MCA-CMS is used with more geometrically complex acoustic-structure systems, the approach has some appeal relative to alternative acoustic-structure CMS methods [18] because MCA-CMS does not require explicit knowledge of subsystem mass and stiffness matrices. This is advantageous because these matrices can be cumbersome to extract from finite element software. A preliminary implementation of MCA-CMS on a three dimensional acoustic-structure system can be found in a conference paper by the authors [19].

2 Theory

Consider a SDOF piston coupled to the one-dimensional acoustic waveguide as shown in Fig. 1. The piston has mass, m_s, and is restrained by a spring of stiffness, k_s, and a viscous damper with a damping coefficient, c_s. The waveguide is filled with fluid with density ρ_0 and speed of sound c_0. The face of the piston has an area A and is located a $x = 0$. The rigid end of the waveguide is at $x = L$. This system is analyzed using the MCA-CMS approach. Broadly speaking, the approach proceeds as follows: 1) Describe the fluid system using a set of Ritz basis vectors and find the associated natural frequencies and modes. 2) Assemble the disjoint fluid-structure system in modal coordinates and enforce the interface constraint using Lagrange multipliers. 3) Perform a frequency response analysis using the complex-valued natural frequencies and modes to find the response of the system for varying levels of acoustic subsystem damping.

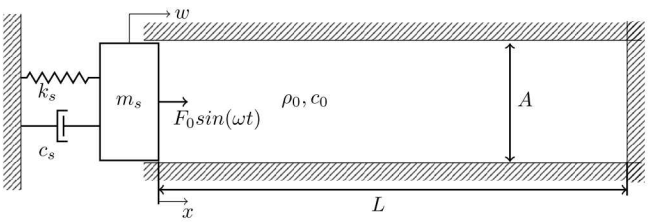

Fig. 1: SDOF piston coupled to one-dimensional closed waveguide

2.1 Ritz Analysis

The objective here is to perform an eigen-analysis in the fluid domain to identify a basis of acoustic natural frequen-

cies and modes that can be used in the MCA-CMS procedure. The fluid mass and stiffness matrices used in the eigenanalysis are found with the expressions for total kinetic and potential energy of an acoustic fluid [7]

$$T_f = \frac{\rho_0 A}{2} \int_0^L v(x,t)^2 dx, \tag{1}$$

$$U_f = \frac{\rho_0 c_0^2 A}{2} \int_0^L \left(\frac{\partial u(x,t)}{\partial x} \right)^2 dx, \tag{2}$$

where $v(x,t)$ and $u(x,t)$ are the fluid particle velocity and displacement, respectively.

The Ritz approach assumes that fluid velocity potential, ϕ, can expressed as a superposition of the products of basis vectors, denoted ψ_j, and generalized velocities, $\dot{z}_j$,

$$\phi(x,t) = \sum_j \psi_j(x) \dot{z}_j(t). \tag{3}$$

In one dimension, the fluid particle velocity is related to velocity potential by $v = \partial\phi/\partial x$. Using the fact that space and time are separated in Eqn. (3), Eqns. (1) and (2) can be written as

$$T_f = \frac{1}{2} \sum_j \sum_k M_{f_{jk}} \dot{z}_j \dot{z}_k, \tag{4}$$

$$U_f = \frac{1}{2} \sum_j \sum_k K_{f_{jk}} z_j z_k, \tag{5}$$

where the elements of the fluid mass and stiffness matrices are calculated from

$$M_{f_{jk}} = \rho_0 A \int_0^L \psi_j'(x) \psi_k'(x) dx, \tag{6}$$

$$K_{f_{jk}} = \rho_0 A c_0^2 \int_0^L \psi_j''(x) \psi_k''(x) dx. \tag{7}$$

Here, the prime notation is used to denote a spatial derivative. Next, a finite number Ritz vectors are chosen, and the fluid natural frequencies and modes are calculated from the associated eigenvalue problem,

$$\left([K_f] - \omega_f^2 [M_f] \right) \{\Phi_f\} = \{0\}, \tag{8}$$

where ω_f and $\{\Phi_f\}$ denote a pair of fluid natural frequencies and modes. The modes are then mass normalized such that $\left[\overline{\Phi}_f\right]^T [M_f] \left[\overline{\Phi}_f\right] = [I]$, where $[I]$ is the identity matrix.

2.1.1 Choice of Ritz Vectors

As discussed by Ginsberg [7, 8], a key consideration in the Ritz analysis of acoustic-structure systems is the choice of appropriate Ritz vectors. Requirements for candidate vectors are that they be linearly independent and kinematically admissible [20]. A number of families of functions can potentially satisfy these requirements (e.g., trigonometric functions, polynomials, Bessel functions). The rigid wall acoustic modes of the duct are a tempting choice of basis functions because they are familiar, easily expressed, and likely to closely approximate the acoustic modes of the coupled system. These modes are given by

$$\psi_j = cos\left(\frac{j\pi x}{L} \right) \quad j = 0,1,2,..., \tag{9}$$

which have corresponding natural frequencies given by $\omega = j\pi c_0/L$. However, recognizing that the velocity of the fluid at the fluid-structure interface is proportional to $\partial\phi/\partial x$, interface compatibility in the coupled system cannot be enforced if all basis vectors are defined such that $\psi'(0) = 0$. This disallows the exclusive use of rigid wall modes as basis functions. An alternative strategy is to use modes with zero pressure at the interface. These so-called *pressure-release modes* are given by

$$\psi_j = sin\left(\frac{(2j+1)\pi x}{2L} \right) \quad j = 0,1,2,..., \tag{10}$$

with natural frequencies of $\omega = (2j+1)\pi c_0/2L$. While pressure-release modes have a non-zero derivative at the interface, their exclusive use will lead to slow convergence and incorrect interface pressures. However, if the coupled response of the structure is of primary interest, it may be possible to obtain accurate results using a basis composed entirely of pressure-release modes [19]. This is convenient for systems with complex geometry because some commercial finite element software packages can easily compute pressure-release natural frequencies and modes.

To circumvent issues with the exclusive use of rigid wall or pressure release modes, it is possible to use a basis that is a combination of the two. Alternatively, it is possible to augment a basis of pressure-release modes with polynomial vectors, e.g.,

$$\psi_j = \left(\frac{L-x}{L} \right)^{j+1} \quad j = 1,2,3,.... \tag{11}$$

Note that the use of a mixed basis can produce some subsystem natural frequencies and modes that have no obvious physical significance. These modes, however, enrich the modal description of the subsystem and enable constraints to be enforced more readily. For the present system, when mixed bases involving open-closed modes and closed-closed modes are used, it is observed that all but the highest one or two fluid subsystem natural frequencies correspond to open-closed natural frequencies of the duct. It is also observed that the largest fluid subsystem natural frequency is usually much higher than the others. Similar eigenvalue behavior is observed when residual flexibility modes (also known as attachment modes) are used in free-interface CMS of purely structural systems [21].

2.2 Modal Coordinate Assembly

Now the modal representations of the acoustic and structural subsystems are assembled. This allows the assignment of modal damping at the subsystem level, which is essential to the subsequent analysis. The procedure begins by assembling the disjoint system

$$\begin{bmatrix}[I] & 0\\ 0 & 1\end{bmatrix}\begin{Bmatrix}\ddot{q}_f\\ \ddot{q}_s\end{Bmatrix}+\begin{bmatrix}[2\zeta_f\omega_f] & 0\\ 0 & 2\zeta_s\omega_s\end{bmatrix}\begin{Bmatrix}\dot{q}_f\\ \dot{q}_s\end{Bmatrix} + \begin{bmatrix}\left[\omega_f^2\right] & 0\\ 0 & \omega_s^2\end{bmatrix}\begin{Bmatrix}q_f\\ q_s\end{Bmatrix}=\begin{Bmatrix}0\\ 0\end{Bmatrix}. \tag{12}$$

Here, $[I]$ is the $N_f \times N_f$ identity matrix where N_f is the total number of fluid basis vectors. Similarly, $[2\zeta_f\omega_f]$ and $\left[\omega_f^2\right]$ are $N_f \times N_f$ diagonal matrices containing the acoustic damping terms and the acoustic natural frequencies squared. Since the structural portion of the system is a SDOF oscillator, it is modeled with a single uncoupled natural frequency, $\omega_s \equiv \sqrt{k_s/m_s}$, and a single viscous damping ratio, $\zeta_s \equiv c_s/2\sqrt{k_s m_s}$. The transformation from physical coordinates to the generalized coordinates, q, is given by

$$\begin{Bmatrix}u\\ w\end{Bmatrix}=\begin{bmatrix}[\psi'] & 0\\ 0 & 1\end{bmatrix}\begin{bmatrix}[\overline{\Phi}_f] & 0\\ 0 & \sqrt{1/m_s}\end{bmatrix}\begin{Bmatrix}q_f\\ q_s\end{Bmatrix}. \tag{13}$$

The equations of motion in Eqn. (12) need to be joined by enforcing the desired constraints in terms of physical coordinates. The constraint equations take the form of

$$[a]\begin{Bmatrix}u_{int}\\ w_{int}\end{Bmatrix}=\begin{Bmatrix}0\\ 0\end{Bmatrix}, \tag{14}$$

where $[a]$ is a boolean constraint matrix and u_{int} and w_{int} are the interface displacements of the fluid and structure. For the present system where displacement compatibility is enforced at $x = 0$, $[a]$ is a 1×2 vector given by $[1,-1]$. Inserting Eqn. (14) into Eqn. (13) gives a set of constraint equations in terms of the generalized coordinates

$$[a]\begin{bmatrix}[\psi'_{int}] & 0\\ 0 & 1\end{bmatrix}\begin{bmatrix}[\overline{\Phi}_f] & 0\\ 0 & \sqrt{1/m_s}\end{bmatrix}\begin{Bmatrix}q_f\\ q_s\end{Bmatrix}=[\hat{a}]\begin{Bmatrix}q_f\\ q_s\end{Bmatrix}=\begin{Bmatrix}0\\ 0\end{Bmatrix}. \tag{15}$$

In the constrained system, the constraint forces are included in the equations of motion. These forces are proportional to the rows of the constraint matrix $[\hat{a}]$, and the constants of proportionality, Λ, are known as Lagrange multipliers [20]. The constraint equation in Eqn. (15) and the equations of motion in Eqn. (12) with the constraint forces are the complete equations of motion for the system

$$\begin{bmatrix}[I] & 0\\ 0 & 1\end{bmatrix}\begin{Bmatrix}\ddot{q}_f\\ \ddot{q}_s\end{Bmatrix}+\begin{bmatrix}[2\zeta_f\omega_f] & 0\\ 0 & 2\zeta_s\omega_s\end{bmatrix}\begin{Bmatrix}\dot{q}_f\\ \dot{q}_s\end{Bmatrix} + \begin{bmatrix}\left[\omega_f^2\right] & 0\\ 0 & \omega_s^2\end{bmatrix}\begin{Bmatrix}q_f\\ q_s\end{Bmatrix}=[\hat{a}]^T\{\Lambda\}, \tag{16}$$
$$[\hat{a}]\begin{Bmatrix}q_f\\ q_s\end{Bmatrix}=\begin{Bmatrix}0\\ 0\end{Bmatrix}.$$

Eqns. (16) are a set of differential-algebraic equations that can be solved by identifying a set of unconstrained degrees of freedom, denoted ξ. This set is related to the complete set of generalized coordinates by

$$\begin{Bmatrix}q_f\\ q_s\end{Bmatrix}=[B]\{\xi\}, \tag{17}$$

where $[B]$ is a transformation matrix that eliminates the constrained degrees of freedom. Using Eqn. (17) and the constraint equations in Eqns. (16), gives

$$[\hat{a}][B]\{\xi\}=\{0\}. \tag{18}$$

For Eqn. (18) to hold for non-trivial values of ξ, $[\hat{a}][B]=[0]$. In linear algebra, $[B]$ is called the nullspace (or kernel) of $[\hat{a}]$.

Substituting Eqn. (17) into the first of Eqns. (16) and premultiplying both sides of the first equation by $[B]^T$ gives

$$\left[\hat{M}\right]\left\{\ddot{\xi}\right\}+\left[\hat{C}\right]\left\{\dot{\xi}\right\}+\left[\hat{K}\right]\{\xi\}=[B]^T[\hat{a}]^T\{\Lambda\}, \tag{19}$$

where $[B]^T[\hat{a}]^T=0$ since $[\hat{a}][B]=[0]$, and where the system matrices are given by

$$\begin{aligned}\left[\hat{M}\right]&=[B]^T\begin{bmatrix}[I] & 0\\ 0 & 1\end{bmatrix}[B],\\ \left[\hat{C}\right]&=[B]^T\begin{bmatrix}[2\zeta_f\omega_f] & 0\\ 0 & 2\zeta_s\omega_s\end{bmatrix}[B],\\ \left[\hat{K}\right]&=[B]^T\begin{bmatrix}\left[\omega_f^2\right] & 0\\ 0 & \omega_s^2\end{bmatrix}[B].\end{aligned} \tag{20}$$

2.3 Complex Modal Analysis

Due to the presence of arbitrary subsystem damping, the natural frequencies and modes resulting from Eqn. (20) will generally be complex-valued. To calculate the steady-state forced response of the system, a complex modal analysis procedure is used. The procedure is outlined here, and a complete description can be found in the work of Patil [22].

First, the non-symmetric system of n second-order ODEs is written as a system of $2n$ first-order ODEs

$$\{\dot{\chi}\} = [S]\{\chi\} + [D]\{R\}, \tag{21}$$

where

$$\{\chi\} = \begin{Bmatrix} \xi \\ \dot{\xi} \end{Bmatrix}, \quad [D] = \begin{bmatrix} [0] \\ \left[\hat{M}\right]^{-1} \end{bmatrix},$$
$$[S] = \begin{bmatrix} [0] & [I] \\ -\left[\hat{M}\right]^{-1}\left[\hat{K}\right] & -\left[\hat{M}\right]^{-1}\left[\hat{C}\right] \end{bmatrix}, \tag{22}$$

and where $\{R\}$ is the forcing vector in the ξ generalized coordinate system. It is related to the forcing vector in physical coordinates, $\{F\}$, via

$$\{R\} = [B]^T \begin{bmatrix} \left[\overline{\Phi}_f\right] & 0 \\ 0 & \sqrt{1/m_s} \end{bmatrix}^T \begin{bmatrix} -\rho_0 c_0^2 [\psi''] & 0 \\ 0 & 1 \end{bmatrix}^T \{F\}, \tag{23}$$

where the fluid portion of $\{F\}$ is in terms of acoustic pressure, p, with the $-\rho_0 c_0^2[\psi'']$ term resulting from the continuity equation for compressible inviscid fluid, $p = -\rho_0 c_0^2 u'$ [7]. Assuming $\{R\} = \{0\}$ and that Eq. (21) has solutions of the form $\{\chi\} = \Xi\{X\}e^{\lambda t}$, where λ is a system eigenvalue, the standard algebraic eigenvalue problem is then,

$$[S]\{X\} = \lambda\{X\}. \tag{24}$$

The eigenvectors associated with Eq. (24) are not orthogonal with respect to the nonsymmetric system matrix $[S]$, but are biorthogonal to the eigenvectors corresponding to the adjoint eigenvalue problem, i.e., $[S]^T\{Y\} = \lambda\{Y\}$. A given pair of eigenvectors, $\{X_i\}$ and $\{Y_j\}$, (known as right and left eigenvectors, respectively) can be normalized accordingly

$$\{\overline{Y_j}\}^{*T}\{\overline{X_i}\} = 2\delta_{ij} \quad (i,j = 1,2,3,...,2n), \tag{25a}$$
$$\{\overline{Y_j}\}^{*T}[S]\{\overline{X_i}\} = 2\lambda_i\delta_{ij} \quad (i,j = 1,2,3,...,2n), \tag{25b}$$

where the superscript $[\circ]^{*T}$ denotes the complex conjugate transpose and δ_{ij} is the Kronecker delta function. The factor of two in these relations simplifies the transition of the system into a second-order form. Solving the system and adjoint eigenvalue problems results in n pairs of complex conjugate eigenvalues and eigenvectors

$$\lambda_k = \alpha_k + i\beta_k \quad \lambda_{n+k} = \alpha_k - i\beta_k, \tag{26a}$$
$$\{\overline{X_k}\} = \{r_k\} + i\{s_k\} \quad \{\overline{X}_{n+k}\} = \{r_k\} - i\{s_k\}, \tag{26b}$$
$$\{\overline{Y_k}\} = \{v_k\} + i\{w_k\} \quad \{\overline{Y}_{n+k}\} = \{v_k\} - i\{w_k\}, \tag{26c}$$

where (k = 1, 2, 3, ..., n). For a given mode index k, the modal force, $\hat{F}_k$, is given by two scaler quantities,

$$\hat{F}_k^a = \{v_k\}^T[D]\{R\}, \tag{27a}$$
$$\hat{F}_k^b = -\{w_k\}^T[D]\{R\}. \tag{27b}$$

The transformation of Eqn. (21) into an equivalent system of n uncoupled second-order equations is now sought. This second-order form is appealing because it facilitates direct analogies to the familiar results of classical modal analysis. However, the transformation requires that $\hat{F}_k^a = 0$. This can be satisfied by first recognizing that scaling an eigenvector by any complex constant, c_k, will return another system eigenvector. It is therefore possible to find a value of c_k that renders a purely imaginary eigenvector when it is multiplied by the original left eigenvector, $\{Y\}_k$. This will ensure that $\hat{F}_k^a = 0$. Setting the complex modulus of c_k to unity will also ensure that the normalization of the eigenvectors is maintained. The desired complex constant is calculated from

$$c_k = \frac{\left(\hat{F}_k^b - i\hat{F}_k^a\right)}{\sqrt{\left(\hat{F}_k^a\right)^2 + \left(\hat{F}_k^b\right)^2}}, \tag{28}$$

and is then multiplied by $\{\overline{Y}_k\}$. Its complex conjugate is multiplied by $\{\overline{X}\}_k$. This results in two transformed sets of biorthonormal eigenvectors with new corresponding values of $\{r_k\}$ $\{s_k\}$, $\{v_k\}$, and $\{w_k\}$. These new values are used to calculate the steady-state complex amplitude response of the generalized coordinates

$$\begin{Bmatrix} \Xi(\omega) \\ \dot{\Xi}(\omega) \end{Bmatrix} = \sum_{k=1}^{n} \frac{\hat{F}_k^b}{\left(\alpha_k^2 + \beta_k^2\right) - \omega^2 - 2\alpha_k i\omega} \times \left(\{r_k\} + \frac{i\omega - \alpha_k}{\beta_k}\{s_k\}\right), \tag{29}$$

where $\hat{F}_k^b$ is now given by

$$\hat{F}_k^b = \left\{\alpha_k\{v_k\} - \beta_k\{w_k\}\right\}^T[D]\{R\}, \tag{30}$$

and the transformation back into physical coordinates in terms of acoustic pressure and structural displacement is

$$\begin{Bmatrix} p \\ w \end{Bmatrix} = \begin{bmatrix} -\rho_0 c_0^2[\psi''] & 0 \\ 0 & 1 \end{bmatrix} \begin{bmatrix} \left[\overline{\Phi}_f\right] & 0 \\ 0 & \sqrt{1/m_s} \end{bmatrix} [B]\{\Xi\}. \tag{31}$$

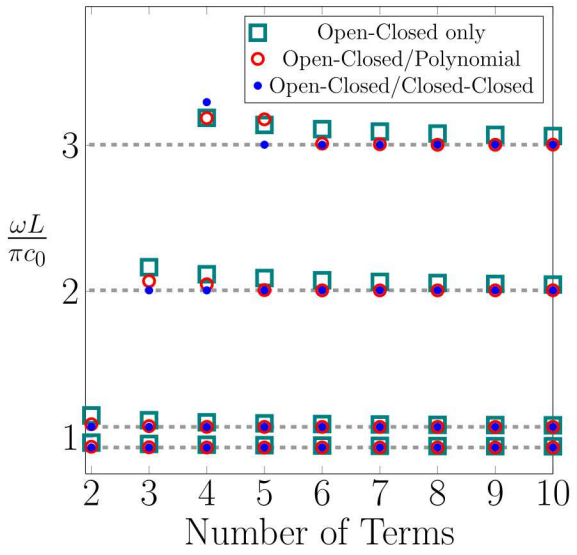

Fig. 2: First three natural frequencies as calculated using three different types of bases (markers) compared to values calculated analytically using Eqn. (32) (dashed lines)

3 Results

3.1 Convergence and Verification

As the number of basis functions is increased, the convergence of the first four natural frequencies can be observed in Fig. 2. Three different types of bases are considered. In each basis, open-closed modes (Eqn. (10)) are used with: 1. no additional basis vectors, 2. additional polynomial basis vectors (Eqn. (11)), and 3. additional closed-closed modes (Eqn (9)). For cases 2 and 3, vectors are added by alternating between the two types beginning with the open-closed modes. Fig. 2 shows results versus the total number of basis vectors with mass ratio $\sigma \equiv m_s/\rho_0 AL = 10$ and uncoupled natural frequency ratio $\omega_s L/\pi c_0 \equiv \eta = 1$. This perfect coincidence of uncoupled natural frequencies results in two coupled natural frequencies with values above and below the uncoupled natural frequency. The first four natural frequencies calculated using the MCA-CMS method are compared to those identified analytically from the characteristic equation [7],

$$\Gamma \equiv \sigma\left((kL)^2 - \left(\frac{\omega_s L}{c_0}\right)^2\right) sin(kL) - kLcos(kL) = 0, \quad (32)$$

where $k \equiv \omega/c_0$. The results show that the most rapid frequency convergence is achieved when the set of closed-open modes are augmented with closed-closed modes. The use of three open-closed modes in conjunction with two closed-closed modes (five vectors total) causes the first four natural frequencies to be well converged. This suggests that, given an efficient basis, it may be possible to achieve sufficient natural frequency convergence using a number of vectors that is one greater than the number of natural frequencies of interest. This is not surprising since the application single constraint equation eliminates one generalized degree of freedom. Given the simplicity of the present problem, retaining more than the minimum number of vectors is not computationally burdensome, so in subsequent results, a total of ten vectors (five open-closed and five closed-closed) are retained. It is noted that similarly good convergence can also be obtained by using a basis consisting of primarily open-closed modes and just one or two closed-closed modes.

The implementation of the frequency response method described in Section 2.3 is checked against closed-form analytical expressions for the undamped case. For a harmonically driven piston with a forcing amplitude of F_0, Ginsberg [7] gives the steady-state response of the mean-square acoustic pressure averaged over the length of the waveguide as

$$p_{av}^2(k) = \frac{F_0^2 kL\,(2kL + sin(2kL))}{8(\Gamma A)^2}, \quad (33)$$

and the amplitude of the corresponding structural response as

$$W(k) = \frac{F_0 L sin\,(kL)}{\rho_0 c_0 A \Gamma}. \quad (34)$$

Fig. 3 compares the frequency response of the structure and the fluid as calculated by the MCA-CMS approach and the analytical expressions. Here, $\sigma = 10$ and $\eta = 1$. For calculation of the mean-square pressure using MCA-CMS, the fluid domain is discretized into 500 segments. The steady-state response of the structure is normalized by the static deflection of the uncoupled piston (i.e., $W_0 = F_0/k_s$). For cases in which the effective stiffness of the fluid is small relative to k_s, the structural FRF will approach unity at the low frequency limit. The spatially averaged mean-square pressure in Fig. 3(b) is normalized by the spatially averaged mean-square pressure due to a static piston deflection,

$$p_{av_0}^2 = \frac{1}{2}\left(\frac{\rho_0 c_0^2 F_0}{L k_s}\right)^2. \quad (35)$$

The two sets of results in Fig. 3 are nearly indistinguishable, which indicates the accuracy of the MCA-CMS implementation. The error curves in Fig. 3 quantify the normalized difference between the frequency domain and MCA-CMS solutions. These curves represent the absolute value of the difference between the frequency domain and MCA-CMS solutions at a given frequency, normalized by the frequency domain solution at that frequency. The error curves confirm that the differences between the two solutions are negligible. Relatively large errors are observed only at resonances and anti-resonances where response amplitudes are not physical due to the absence of damping.

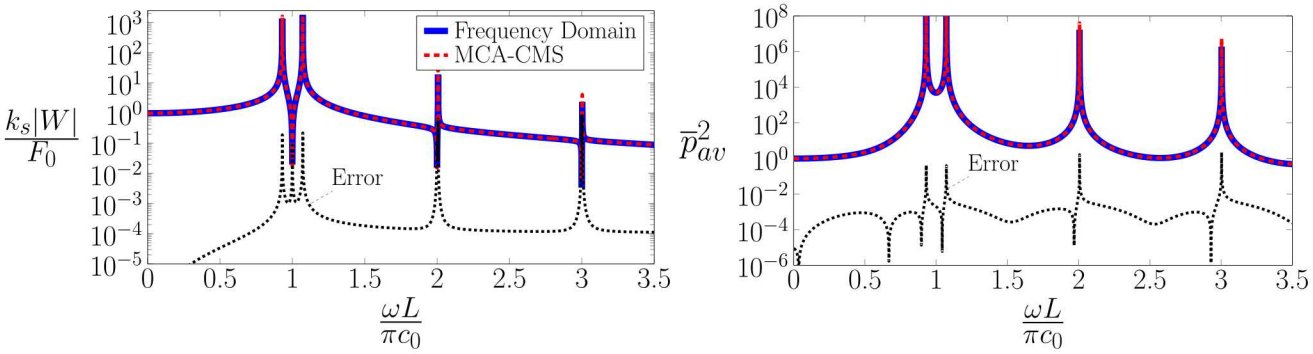

Fig. 3: (a) Structural FRF and (b) normalized mean-square cavity pressure averaged over the length of the waveguide ($\overline{p}^2_{av} = p^2_{av}/p^2_{av_0}$) for $\sigma = 10$, $\eta = 1$, and no damping

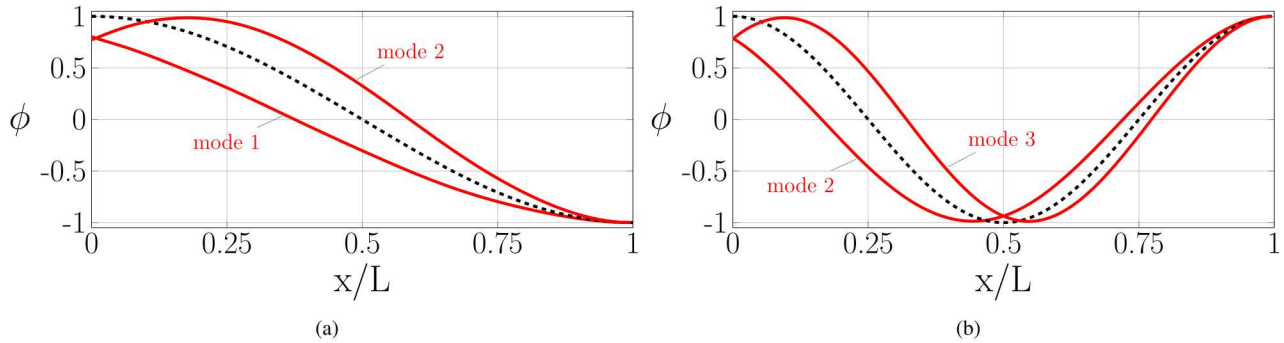

Fig. 4: Coupled mode shapes (solid) compared to corresponding closed-closed mode (dashed) for $\sigma = 1$, (a) $\eta = 1$, and (b) $\eta = 2$

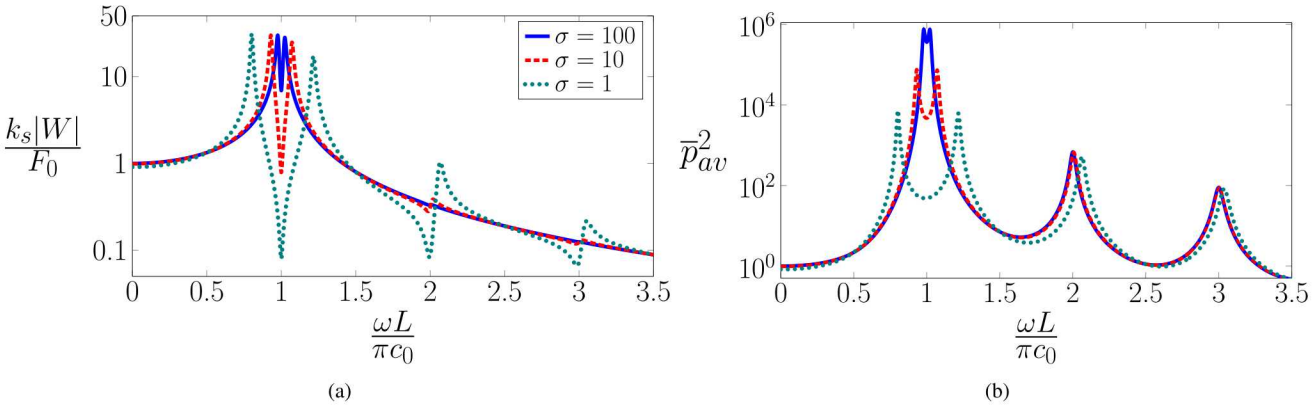

Fig. 5: (a) Structural FRF and (b) normalized mean-square cavity pressure averaged over the length of the waveguide for $\eta = 1$ and three different mass ratios

Fig. 3 further illustrates the fundamental effects of acoustic-structure coupling; namely, when an uncoupled structural and acoustic natural frequency exactly coincide, two system resonances appear at frequencies above and below the uncoupled natural frequency. For the present system, the extent to which resonant frequencies separate due to coupling effects depends on the proximity of uncoupled frequencies and the structure-to-fluid mass ratio. This behavior is reminiscent of that of a classical vibration absorber, where in this case, the piston is the primary mass and the fluid is

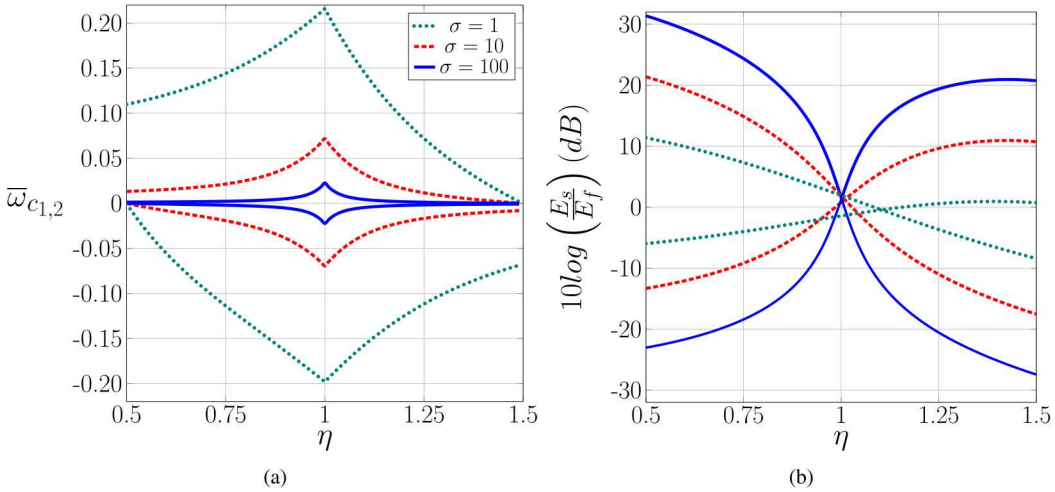

(a) (b)

Fig. 6: (a) Normalized coupled natural frequencies and (b) modal energy ratio versus uncoupled frequency ratio for three different mass ratios

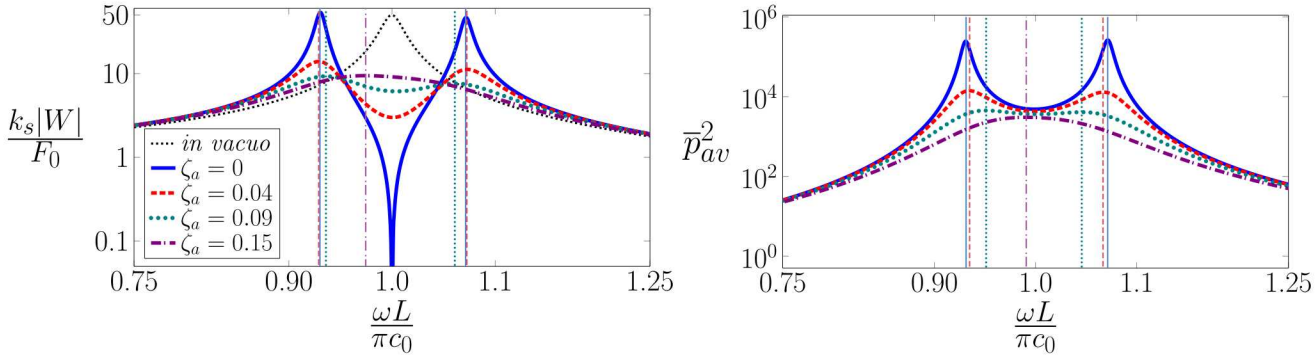

(a) (b)

Fig. 7: (a) Structural FRF and (b) mean-square pressure averaged over the length of the waveguide for $\eta = 1$ and three different acoustic damping levels and $\zeta_s = 0.01$. Vertical lines indicated resonant frequencies.

analogous to the secondary mass.

3.2 Acoustic-Structure Resonances

Before considering the influence of acoustic damping, the effects of acoustic-structure coupling in the undamped case are observed in more detail. In addition to altering system natural frequencies, coupling causes changes to the acoustic modes. These changes are most profound for small mass ratios. As the piston mass increases relative to the mass of the fluid, the face of the piston acts increasingly like a rigid wall and the coupled modes shapes will approach that of a rigid wall waveguide. Fig. 4(a) and (b) respectively show the two coupled pressure mode shapes when $\eta = 1$ and $\eta = 2$. The mode shapes are normalized to unity and compared to the corresponding closed-closed mode of the waveguide. To more clearly observe coupling effects, σ is set to unity. Fig. 4(a) shows that relative to the closed-closed mode, the first coupled mode is similar in shape, but has lower amplitude at the piston interface. This is expected given that the non-zero velocity of the interface will not result in a pressure maximum. While the first coupled mode varies monotonically down the length of the waveguide, the second coupled mode obtains a pressure maximum at $x/L \approx 0.2$. In Fig. 4(b), the uncoupled structural natural frequency corresponds to the second non-zero natural frequency of the rigid waveguide. Here, because of the acoustic resonance at $\omega = \pi c_0/L$, the coupled modes are the second and third modes of the system and are comparable to the second $j = 2$ closed-closed shape. It is observed that acoustic-structure coupling has the effect of shifting the nodes of the coupled mode shapes, with the nodes closest to the piston undergoing the greatest shift. In fact, all of the coupled modes tend to approach the closed-closed shape with increasing distance down the waveguide [23].

Fig. 5 shows the structural FRF and the spatially averaged mean-square pressure response for σ = 1, 10, and 100 when $\eta = 1$, $\zeta_s = 0.01$, and $\zeta_f = 0$. Increasing mass

ratio has the effect of decreasing the frequency separation of the coupled resonances, and changes in mass ratio affect the amplitudes of the coupled structural and fluid resonances in different manners. In the structural FRF, changing mass ratio has little influence on normalized amplitudes of the coupled resonances. However, the higher acoustically-dominated structural resonances are only significant for low mass ratios. These trends are reversed in the fluid domain. For the coupled resonances, the normalized average mean-square pressure is considerably higher when the mass ratio is high; yet, changing the mass ratio has little influence on amplitude of the higher-order acoustic resonances. Note that the frequencies at which these higher-order resonances occur shift higher when $\sigma = 1$. This is because at low mass ratios, the stiffness provided by the acoustic fluid is not negligible relative to the mechanical stiffness.

Fig. 6(a) plots system natural frequencies normalized by the nearest uncoupled natural frequency. These normalized frequencies can be interpreted as the fractions by which a given natural frequency is shifted due to acoustic-structure coupling. Results are shown for σ =1, 10, and 100 across η values from 0.5 to 1.5. As anticipated, the largest frequency shifts occur when the uncoupled natural frequencies are close and the mass ratio is small. For $\sigma = 100$, the uncoupled natural frequencies must be nearly equivalent to observe appreciable changes in the coupled natural frequencies. In the case of $\sigma = 1$, coupling causes significant shifts in natural frequency even when the uncoupled natural frequencies are not especially close.

Fig. 6(b) considers the energy content of the coupled modes. When the system is not strongly coupled, system modes are dominated by either structural or acoustic content, whereas strongly coupled modes exhibit non-negligible energy content in both the fluid and structure degrees of freedom. The ratio of structural energy, E_s, to fluid energy E_f, in a given pair of modes [4] is

$$\frac{E_s}{E_f} = \frac{\sigma c_0^2 \Phi_{c_s}^2}{\{\Phi_{c_f}\}^T \{\Phi_{c_f}\}}. \tag{36}$$

Here, Φ_{c_s} and Φ_{c_f} represent the structural and fluid portions of a coupled mode, where the structural portion has units of displacement and the fluid portion has units of velocity potential. This ratio is plotted on decibel scale in Fig. 6(b) across η values from 0.5 to 1.5. Mass ratios of 1, 10, and 100 are again considered. The results indicate the greatest parity between structural and fluid energy occurs when the uncoupled natural frequencies are nearly coincident. When the uncoupled natural frequencies are not in close proximity, modes corresponding to higher values of σ are more strongly dominated by either structural or acoustic energy, with positive and negative decibel values indicating structurally and acoustically dominated modes, respectively. For $\sigma = 1$, the point of greatest parity between the structural and fluid energy occurs when $\eta \approx 1.1$. This is in contrast to the coupled natural frequency behavior in Fig. 6(a) where the largest coupled frequency shifts occur at $\eta = 1$ regardless of mass ratio. This indicates that coupling influences system eigenvalues and eigenvectors somewhat differently.

3.3 Varying Acoustic Subsystem Damping

Now the effects of acoustic subsystem damping on the system response are considered with the response of the structural subsystem being of most interest. Unless otherwise noted in the subsequent results, the structural subsystem damping is assumed to be $\zeta_s = 0.01$. Since all physical structures have some amount of damping, the use of a non-zero structural damping adds realism to the analysis. The choice of $\zeta_s = 0.01$, while customary, is arbitrary. A different choice of ζ_s would of course change the results. Nevertheless, it is believed that the qualitative system behavior persists regardless of the choice of structural damping. This should be especially true as long as the structural damping remains low. These assertions are supported by research involving the effects of primary structure damping on the response of TMDs [14].

To observe the resonant behavior of the coupled acoustic-structure modes as damping is added to the acoustic subsystem, consider Fig. 7 where $\sigma = 10$, $\eta = 1$, and $\zeta_s = 0.01$. Here, vertical lines are used to indicate the resonant frequencies of the corresponding response curves. When $\zeta_f = 0$, the structural FRF exhibits two pronounced resonance peaks and a distinct anti-resonance. The first of these resonance peaks has a maximum amplitude that is slightly higher than the corresponding *in vacuo* structural resonance (i.e., $Q_0 \approx 1/2\zeta_s = 50$) while the second coupled resonance is slightly lower. The spatially averaged mean-square pressure response curve has two resonances at nearly the exact same frequencies as the structural FRF. Due to the exchange of energy between the fluid and the structure, these acoustic resonances are bounded even though $\zeta_f = 0$. When $\zeta_f = 0.04$, both the fluid and structural resonances show a significant reduction in amplitude. There is also a slight change in the resonant frequencies. The first structural resonance shifts from $\omega L/\pi c_0 = 0.930$ to $\omega L/\pi c_0 = 0.929$ while the second structural resonance shifts from $\omega L/\pi c_0 = 1.071$ to $\omega L/\pi c_0 = 1.073$, resulting in the resonances being slightly more separated than they are when $\zeta_f = 0$. The fluid resonant frequencies, however, shift such that they become less separated than they are when $\zeta_f = 0$. When $\zeta_f = 0.09$, the response amplitudes in both the structure and the fluid further decrease making the coupled resonance peaks very broad. The resonant frequency separation in both the fluid and the structure is less than it is when $\zeta_f = 0$, with the decrease in resonant frequency separation being more pronounced in the fluid. Finally, when $\zeta_f = 0.15$, the responses exhibit a single resonance peak that, in the case of the structure, has a greater amplitude than either of the of the resonance peaks when $\zeta_f = 0.09$. In the case of the fluid, the $\zeta_f = 0.15$ resonance peak has the lowest amplitude and is found at a frequency of $\omega L/\pi c_0 = 0.991$ whereas the corresponding structural resonance occurs at $\omega L/\pi c_0 = 0.974$.

It is clear from Fig. 7 that changes to energy dissipation in the acoustic domain result in nuanced changes to the fre-

quency response of both the structure and the fluid. Fig. 8 shows these changes for $\sigma = 10$ and uncoupled frequency ratios of 0.95, 1.0 and 1.05. The left-hand panels of Fig. 8 track system resonant frequency against increases in acoustic damping. The resonant frequencies are overlaid onto the corresponding system natural frequencies (the imaginary part of the complex eigenvalue). The structural resonant amplitudes are shown with a color scale and are normalized by the corresponding resonant amplitude of the *in vacuo* structural system, $Q_0 = (2\zeta_s\sqrt{1-2\zeta_s^2})^{-1}$. All frequencies are normalized by the first non-zero acoustic natural frequency of the closed-closed waveguide. The right-hand panels plot system damping which is given by the ratio of the real part of the system eigenvalue to the imaginary part.

Observing the behavior of the coupled natural frequencies in Fig. 8 reveals that their separation tends to decrease as acoustic damping is increased. In fact, for uncoupled frequency ratios of 0.95 and 1.0, there exists an acoustic damping level at which the coupled frequencies coincide. However, this same behavior does not exist when $\eta = 1.05$. In all cases, the resonant frequencies closely follow the curve representing the imaginary portion of the eigenvalue when acoustic damping is low.

The system damping curves in Fig. 8 provide additional insight into the system resonant behavior. In Fig. 8(d), $\eta = 1$ and it can be observed that the total damping $(\zeta_s + \zeta_a)$ is effectively split between the two modes for low-to-moderate values of acoustic damping,. This is true even when the vast majority of the damping resides within the fluid. Because the modes are well coupled, energy is exchanged and dissipated efficiently between the modes. However, near $\zeta_a = 0.17$, there is a point at which the real parts of the system eigenvalues abruptly diverge. As acoustic damping increases beyond this point, one mode becomes much more heavily damped while the other becomes more lightly damped. In the response, this results in a single resonance peak that increases in amplitude as acoustic damping is increased. Another feature of the system behavior is that beyond the acoustic damping levels at which the real parts of the system eigenvalues diverge, the total system damping is noticeably less than the total subsystem damping. The behavior in which the real parts of the system eigenvalues closely coincide for low values of ζ_a and then abruptly diverge seems to be a feature of well-coupled systems (i.e., $\eta \approx 1$) with larger mass ratios. This is evidenced in Fig. 9 where the system eigenvalues and resonant behavior are shown for $\sigma = 1$ and $\sigma = 100$ with $\eta = 1$. When $\sigma = 1$, the real parts of the system eigenvalues slowly diverge with increasing acoustic damping. When $\sigma = 100$, the divergence is pronounced and sudden.

From Figs. 8 and 9 alone, it is not entirely clear how the uncoupled natural frequency ratio affects $\zeta_{f_{cr}}$, the acoustic damping at which one of the coupled resonances abruptly disappears. Fig. 10 shows this relationship for $\sigma = 1$, 2, 10, and 100, and the trends are consistent with those observed for the energy ratios of the coupled modes (Fig. 6(b)). Specifically, the highest values of $\zeta_{f_{cr}}$ occur when parity between the structural and fluid modal energy is greatest. In the energy ratio results, it is observed that the point of greatest parity shifts toward higher uncoupled natural frequency ratios when mass ratio is low. This is again observed in the $\zeta_{f_{cr}}$ results, suggesting that the transition from two coupled resonances to one depends on the coupled mode shapes, and not the system natural frequencies.

The behavior of the structural resonant amplitudes with increasing acoustic damping is observed in Fig. 11 for several different mass ratios with $\eta = 1$. Curves corresponding to $\zeta_s = 0.005$ (dashed) and $\zeta_s = 0.01$ (solid) are shown. The acoustic damping is normalized by the assumed structural damping and the resonant amplitudes are normalized by the resonant amplitude of the *in vacuo* structural system, Q_0. Parts (a) and (b) of Fig. 11 show the amplitudes of the first and second resonant peaks, respectively. Across the two levels of structural damping, the results show good qualitative agreement, and at low levels of acoustic damping, the two sets of results agree quantitatively as well.

When $\sigma = 1$ and acoustic damping is low, the first resonance is more than 10% higher than the corresponding *in vacuo* resonance. For $\sigma > 1$ and very low levels of acoustic damping, the two coupled resonance peaks have amplitudes that approximate the amplitude of corresponding *in vacuo* resonance. When $\sigma = 1$, the amplitudes of both resonances decrease monotonically with increasing acoustic damping. For the other values of σ, there exists a value of acoustic damping that minimizes the amplitude of the first resonance. Beyond this damping value, the amplitude of the first resonance increases. For the σ values considered, the value of acoustic damping that minimizes the first resonance is near, but not exactly, the value at which the second resonance disappears. For example, with $\sigma = 100$ and $\zeta = 0.01$, the first resonance is minimized when $\zeta_f/\zeta_s \approx 3.5$ while the second resonance disappears at $\zeta_f/\zeta_s \approx 3$. When ζ_f approaches unity (i.e., $\zeta_a/\zeta_s \approx 10^2$ in the $\zeta_s = 0.01$ case) the $\sigma = 10$ and 100 curves exhibit a local maximum beyond which further increases in acoustic damping cause small decreases in amplitude.

The results have shown that increasing acoustic damping in an acoustic-structure system will first increase the separation between the resonance frequencies in the frequency response of both structure and the fluid. Additional increases in acoustic damping then cause the separation between the coupled resonance frequencies to decrease below the initial separation. In Fig. 12 the (a) minimum and (b) maximum resonant frequency separation is plotted against the uncoupled natural frequency separation for $\zeta_s = 0.01$. The resonant frequency separation is normalized by the separation when $\zeta_f = 0$. Fig. 12(a) shows that the minimum frequency separation of the coupled resonances depends heavily on the uncoupled frequency separation. For the cases in which $\sigma > 1$, the lowest minimum frequency separations occur when $\eta \approx 1$. Fig. 12(b) shows a somewhat different trend. Here, the largest resonant frequency separations occur when the uncoupled natural frequencies are proximate, but not equivalent. In any case, the increases in resonant frequency separation are relatively small and do not exceed 5%.

4 Conclusion

The complicated relationships between acoustic damping and system response are investigated in the context of a simple acoustic-structure system. The system is modeled using an approach that adapts dynamic substructuring techniques for use with acoustic-structure systems. The acoustic subsystem is modeled using a Ritz series approach employing a mixed set of basis vectors. It is shown that a mixed set of pressure-release and rigid wall modes provides an efficient basis for the present system. While attention is restricted to a one dimensional system, the modeling approach can, in principle, be applied to geometrically complex two and three dimensional systems.

Results show that as acoustic damping is increased in the presence of acoustic-structure coupling, the frequencies and amplitudes of the coupled resonances undergo a sequence of changes. For low levels of acoustic damping, the two coupled resonance peaks have amplitudes that approximate the amplitude of the corresponding *in vacuo* resonance. Additionally, the frequency separation between the coupled resonance peaks depends on the mass ratio between the structure and fluid as well as the ratio of uncoupled natural frequencies. As acoustic damping increases, the amplitude of the coupled resonances decreases dramatically while the frequency separation between the resonances increases slightly. As acoustic damping increases even further, the separation between the resonant frequencies decreases considerably. Finally, at some critical value of acoustic damping, one of the resonances abruptly disappears, leaving just a single resonance. Counterintuitively, increasing acoustic damping beyond this point tends to increase the amplitude of the remaining resonance peak. This sequence of response behavior is similar to what has been observed in TMDs as the damping of the attachment mass is increased.

When faced with acoustic-structure coupling in a fluid-filled test structure, system identification and model correlation efforts can be challenging. Further, the results indicate that a simple introduction of acoustic damping material is not a viable method for recovering the *in vacuo* response of the structure. Nevertheless, the present results can help analysts and experimentalists identify acoustic-structure resonances, explain discrepancies in their test/model correlations, and anticipate how changes to the fluid cavity might influence the resonant behavior of test structures.

Acknowledgements

R. B. Davis gratefully acknowledges the financial support of Sandia National Labs, contract 1764414. Sandia National Laboratories is a multimission laboratory managed and operated by National Technology & Engineering Solutions of Sandia, LLC, a wholly owned subsidiary of Honeywell International Inc., for the U.S. Department of Energys National Nuclear Security Administration under contract DE-NA0003525. This paper describes objective technical results and analysis. Any subjective views or opinions that might be expressed in the paper do not necessarily represent the views of the U.S. Department of Energy or the United States Government.

References

[1] Ewins, D. J., 1984. *Modal testing: theory and practice*, Vol. 15. Research studies press Letchworth.

[2] Davis, R. B., 2008. "Techniques to assess acoustic-structure interaction in liquid rocket engines". PhD thesis, Duke University, Durham, North Carolina.

[3] Inman, D. J., 2001. *Engineering Vibration*. Prentice-Hall, Upper Saddle River, NJ.

[4] Pan, J., and Bies, D. A., 1990. "The effect of fluid-structural coupling on sound waves in an enclosure: Theoretical part". *Journal of the Acoustic Society of America,* **87**(2), pp. 691–707.

[5] Schultz, R., and Pacini, B., 2017. "Mitigation of structural-acoustic mode coupling in a modal test of a hollow structure". In *Rotating Machinery, Hybrid Test Methods, Vibro-Acoustics & Laser Vibrometry, Volume 8*. Springer, pp. 71–84.

[6] Davis, R., 2017. "A simplified approach for predicting interaction between flexible structures and acoustic enclosures". *Journal of Fluids and Structures,* **70**, pp. 276–294.

[7] Ginsberg, J. H., 2010. "On Dowells simplification for acoustic cavity-structure interaction and consistent alternatives". *The Journal of the Acoustical Society of America,* **127**(1), pp. 22–32.

[8] Ginsberg, J. H., 2010. "Implementation of a constrained Ritz series modeling technique for acoustic cavity-structural systems". *The Journal of the Acoustical Society of America,* **128**(5), pp. 2562–2572.

[9] Bokil, V. B., and Shirahatti, U. S., 1994. "A technique for the modal analysis of sound-structure interaction problems". *Journal of Sound and Vibration,* **173**(1), pp. 23–41.

[10] Kruntcheva, M. R., 2006. "Acoustic-structural responances of thin-walled structure-gas systems". *ASME Journal of Vibration and Acoustics,* **128**, pp. 722–731.

[11] Ribeiro, P. M. V., and Pedroso, L. J., 2010. "Solution of the dynamic interaction problem between a framed structure and an acoustic cavity using imposed deformation functions at the interface". *Mathematical Problems in Engineering,* **2010**.

[12] Davis, R. B., Virgin, L. N., and Brown, A. M., 2008. "Cylindrical shell submerged in bounded acoustic media: A modal approach". *AIAA Journal,* **46**(3), pp. 752–763.

[13] Rana, R., and Soong, T., 1998. "Parametric study and simplified design of tuned mass dampers". *Engineering structures,* **20**(3), pp. 193–204.

[14] Ghosh, A., and Basu, B., 2007. "A closed-form optimal tuning criterion for tmd in damped structures". *Structural Control and Health Monitoring,* **14**(4), pp. 681–692.

[15] de Klerk, D., Rixen, D. J., and Voormeeren, S. N., 2008. "General framework for dynamic substructur-

ing: History, review, and classification of techniques". *AIAA Journal,* **46**(5), pp. 1169–1181.

[16] Allen, M. S., Mayes, R. L., and Bergman, E. J., 2010. "Experimental modal substructuring to couple and uncouple substructures with flexible fixtures and multipoint connections". *Journal of Sound and Vibration,* **329**(23), pp. 4891–4906.

[17] Ginsberg, J. H., 2010. "Derivation of a Ritz series modeling technique for acoustic cavity-structural systems based on a constrained hamiltons principle". *The Journal of the Acoustical Society of America,* **127**(5), pp. 2749–2758.

[18] Junge, M., Brunner, D., Becker, J., and Gaul, L., 2009. "Interface-reduction for the craig–bampton and rubin method applied to fe–be coupling with a large fluid–structure interface". *International Journal for Numerical Methods in Engineering,* **77**(12), pp. 1731–1752.

[19] Davis, R. B., and Schultz, R., 2018. "Coupling acoustic-structure systems using dynamic substructuring". In *Dynamics of Coupled Structures, Volume 4*. Springer, pp. 183–190.

[20] Ginsberg, J. H., 2001. *Mechanical and Structural Vibrations Theory and Applications*. Wiley, New York.

[21] Davis, R. B., and Fulcher, C. W., 2014. "Framework for optimizing the vibroacoustic response of component loaded panels". *AIAA Journal,* **53**(1), pp. 265–272.

[22] Patil, M. J., 2000. "Decoupled second-order equations and modal analysis of a general non-conservative system". In AIAA 2000-1654 AIAA Dynamics Specialists Conference. Atlanta, Georgia.

[23] Dowell, E. H., 2010. "Comment on "On Dowell's simplification for acoustic cavity-structure interaction and consistent alternatives"". *The Journal of the Acoustical Society of America,* **128**(1), pp. 1–2.

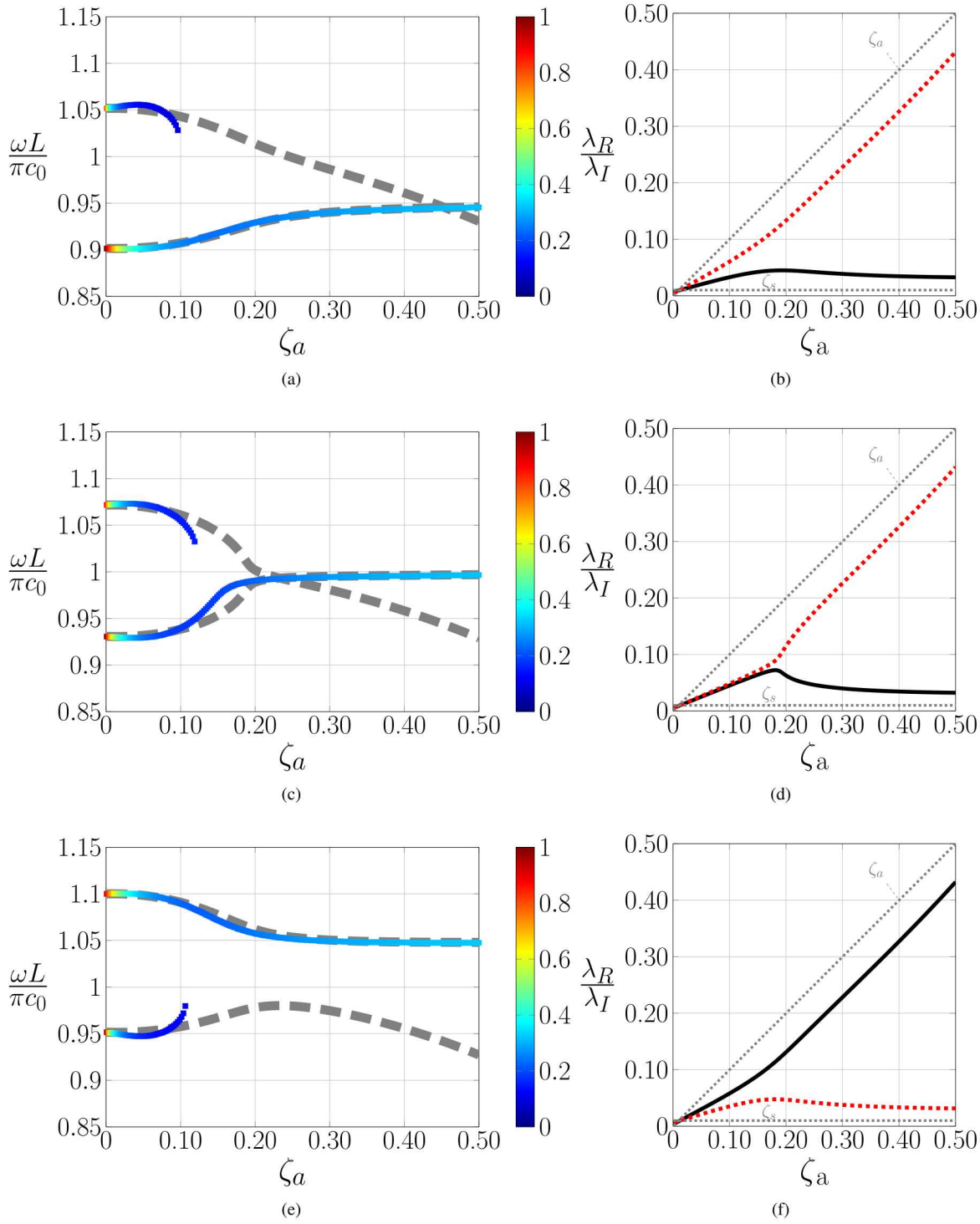

Fig. 8: (Left) normalized resonant frequencies and amplitudes versus acoustic subsystem damping ratio and overlaid on the normalized imaginary parts of the system eigenvalues. (Right) Ratio of real to imaginary parts of first two system eigenvalues versus acoustic subsystem damping ratio. Subsystem damping level are indicated with dotted lines. (a) and (b) $\sigma = 10$, $\eta = 0.95$; (c) and (d) $\sigma = 10$, $\eta = 1$; (e) and (f) $\sigma = 10$, $\eta = 1.05$.

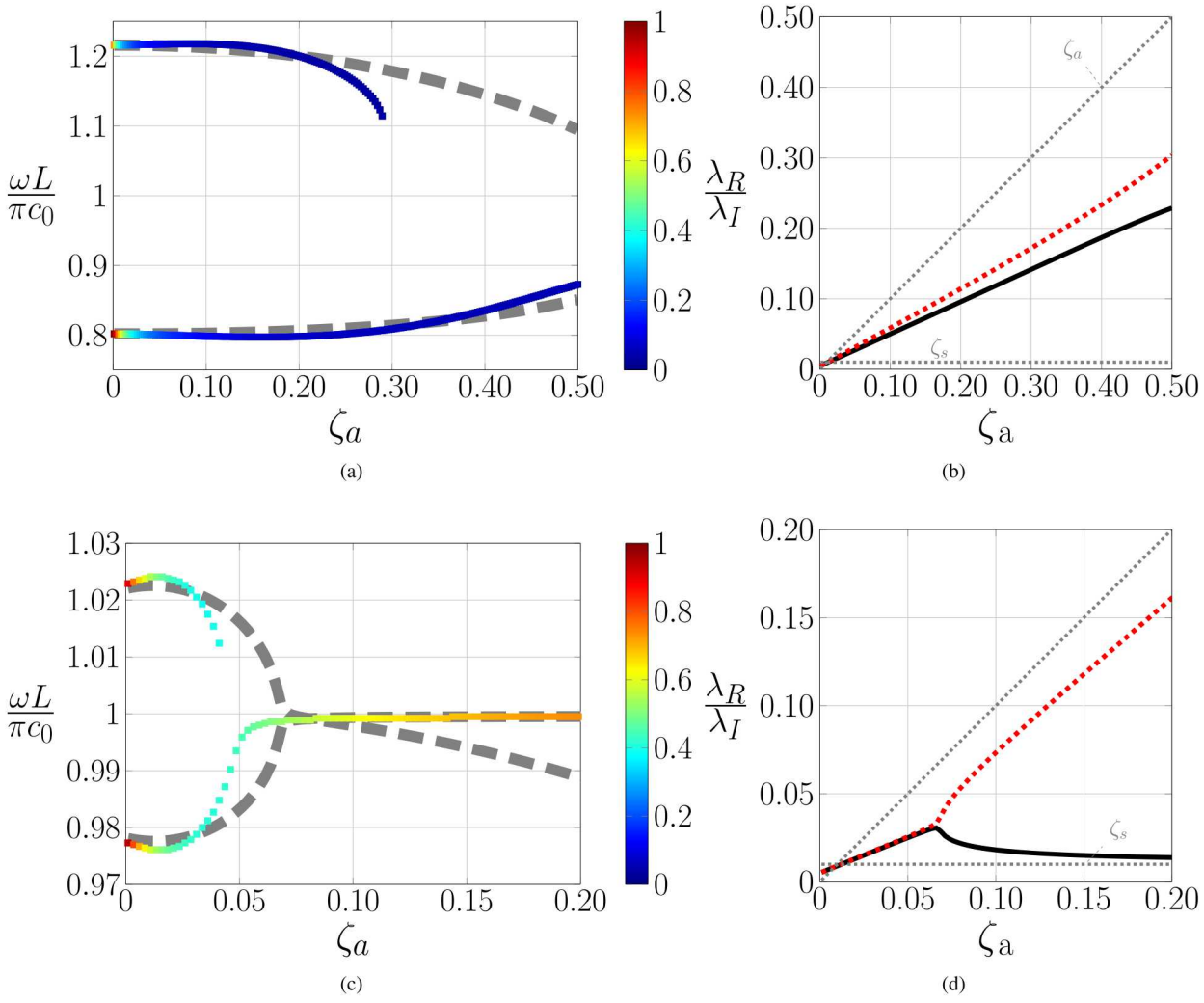

Fig. 9: (Left) normalized resonant frequencies and amplitudes versus acoustic subsystem damping ratio and overlaid on the normalized imaginary parts of the system eigenvalues. (Right) ratio of real to imaginary parts of first two system eigenvalues versus acoustic subsystem damping ratio. Subsystem damping level are indicated with dotted lines. (a) and (b) $\sigma = 1, \eta = 1$; (c) and (d) $\sigma = 100, \eta = 1$.

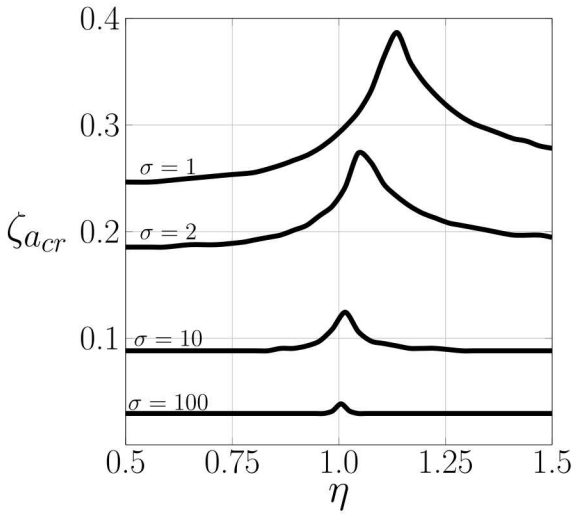

Fig. 10: Acoustic damping ratio at which second resonance disappears versus uncoupled frequency ratio for four different mass ratios and $\zeta_s = 0.01$

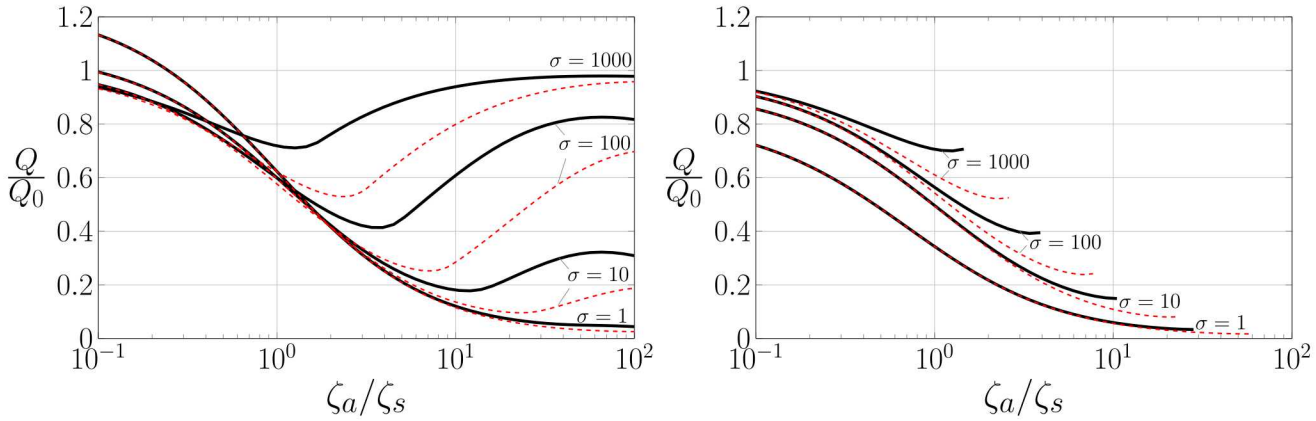

Fig. 11: Normalized resonant amplitudes for versus subsystem damping ratio for four different mass ratios with $\zeta_s = 0.01$ (solid) and $\zeta_s = 0.005$ (dashed) (a) first system resonance (b) second system resonance.

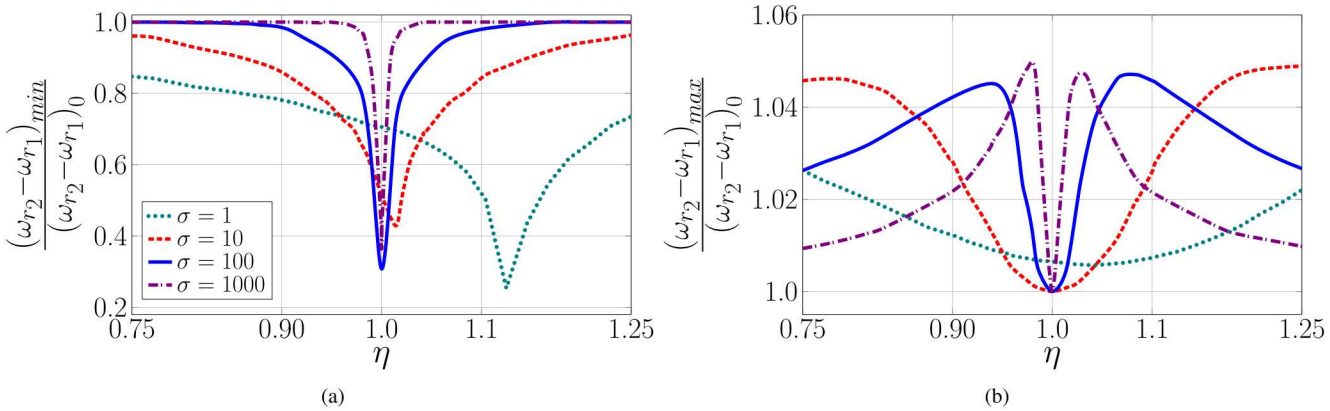

Fig. 12: (a) Minimum (b) maximum resonant frequency separation, $(\omega_{r_2} - \omega_{r_1})$, normalized by the resonant frequency separation with $\zeta_a = 0$, $(\omega_{r_2} - \omega_{r_1})_0$. Results are shown versus uncoupled frequency ratio for four different mass ratios.